

Research Article

Experimental and Numerical Evaluation of Perfobond Rib Shear Connectors Embedded in Recycled Aggregate Concrete

Zhenxuan Yu,¹ Shaohua He ¹, Ayman S. Mosallam,² Shuo Jiang,³ and Wenxian Feng¹

¹School of Civil and Transportation Engineering, Guangdong University of Technology, Guangzhou, Guangdong 510006, China

²Department of Civil & Environmental Engineering, University of California, Irvine, CA 92697, USA

³China Railway Guangzhou Group Co., Ltd., Guangzhou 510000, China

Correspondence should be addressed to Shaohua He; hesh@gdut.edu.cn

Received 17 August 2019; Revised 4 November 2019; Accepted 3 December 2019; Published 6 January 2020

Academic Editor: Giuseppe Quaranta

Copyright © 2020 Zhenxuan Yu et al. This is an open access article distributed under the Creative Commons Attribution License, which permits unrestricted use, distribution, and reproduction in any medium, provided the original work is properly cited.

In this paper, the use of recycled aggregate concrete (RAC) for the upper slabs in steel-concrete composite beams is proposed. Perfobond rib connector (PBL), a relatively new type of shear connectors, has been widely used to ensure composite action between the steel and concrete elements in composite beams. For the past decades, several studies on assessing the performance of PBLs have been conducted, but very few focused on the PBLs that are embedded in RAC slabs. This paper presents results of an experimental and numerical simulation study that focused on characterizing the behavior of PBL fabricated using RAC. In the experimental program, a total of six standard push-out specimens, divided into three groups, were fabricated and loaded to failure. Test results indicated that the ductility of the PBLs using RAC materials decreased as the perforated steel plate thickness decreased, while the PBL ultimate strength increased by 4.3% and 12.8% for steel plate thicknesses of 10.0 mm and 12.0 mm, respectively, as compared to specimens with 8.0 mm steel plate thickness. Finite element (FE) models for PBLs embedded in RAC were developed, and numerical results were validated by corresponding experimental results. An extensive parametric numerical analysis was conducted to assess the effects of different parameters such as transverse steel rebar diameter and perforated steel plate strength and thickness on the performance of such connectors. Numerical simulation results showed that the PBL ultimate strength obtained based on the perforated plate fracture failure mode increases linearly as the steel rebar diameter increases. Also, numerical results indicated that as steel plate strength and thickness increase, failure mode changes from steel plate fracture to rupture of reinforced concrete dowels. Furthermore, existing published analytical formulas for predicting behavior of PBLs were assessed via a comparison with experimental and numerical results developed in this study. The outcomes of this study contribute in providing fundamental knowledge in a new sustainable application of PBL in steel-concrete composite beams with RAC slabs.

1. Introduction

The reuse of construction and demolition (C&D) waste has become a crucial strategy for achieving sustainable construction systems. According to the National Bureau of Statistics of China published in 2013, about 16 to 24 billion tons of concrete are being used in China [1]. Currently, the recycling rate of C&D waste in China does not exceed 5%–10%. There are several reasons for the low rate of using recycled C&D materials, including (i) absence of incentives of using such materials, (ii) low demand for recycled materials as compared to natural aggregates that discourage investors of expanding and developing more recycling

plants, (iii) doubts of engineers and contractors on the quality assurance of recycled materials, and (iv) lack of standards and code provisions related to the use of high potential materials. More details on the use in the recycled construction materials including concrete aggregates are described in the 2018 Technical Assistance Consultant's Report prepared by AECOM for the PRC Ministry of Housing and Urban-Rural Development and the Asian Development Bank [1]. Recently, recycled aggregate concrete (RAC), reusing aggregates from the C&D concrete, are used in different load-bearing structural applications.

The use of RAC offers several advantages including the ease of waste disposal crisis through recycling C&D

materials, preserving natural aggregate resources, and reducing cost of waste storage [2]. However, due to the large short- and long-term deformations and significant scatter of the mechanical properties, the application of RAC has been primarily limited to the pavement base, retaining walls, and other nonstructural fields. To date, advanced concrete technology has significantly improved both quality and stability of RAC, which promotes extensive usage of RAC as structural materials, such as the filling material for concrete-filled steel tubes (CFSTs), reinforced concrete beams and columns, and many other engineering practices [3].

Predominantly, the efficiency of a composite beam fabricated using RAC lies in generating composite action between the steel and RAC elements. Headed studs are the most popular shear connectors for achieving the compound actions between different material elements. However, such connectors have some limitations in the cases of fatigue and specified conditions related to electrical requirements at the site [4]. In order to find a substitution and overcome the drawbacks of the steel studs, an innovative type of shear connector, namely, perfobond rib connector (PBL), resisting loads via a reinforced concrete dowel inside the steel plate holes, was proposed by German company *Leonhard, Andrea and Partners* in 1987 [5]. Figure 1 shows the composite beam installed with PBL connectors. Compared to conventional steel studs, PBL exhibits higher ultimate resistance, easier installation, and better fatigue performance [6–11]. For this reason, PBL connectors are being utilized as an alternative and effective solution for building or bridge structures subjected to severe live loads or special service conditions.

In the past few years, results of several studies that focused on characterizing structural behavior of PBL have been published. In general, there are two main methods to effectively characterize the performance of PBL connectors, namely; (i) finite element (FE) simulations and (ii) push-out tests. As compared to push-out tests, numerical simulation can be a cost-effective alternative in the case that experimental data are available for validating their results. Kraus and Wurzer [12] explored the possibility of modeling PBL behavior using the ADINA computer code. Numerical results indicated that the FE analysis is very suitable for identifying the behavior of complex systems like PBL's concrete dowels. Oguejiofor and Hosain [13] simulated the behavior of PBLs by varying plate thickness, hole number and geometry and steel reinforcement, as well as concrete compressive strength. ANSYS's Solid65 and Shell41 elements were selected in order to simulate the behavior of both concrete slab and perforated plate, respectively. Their findings indicated that numerical modeling technique can predict well the behavior of PBLs under a concrete-related failure mode.

Al-Darzi et al. [14] utilized nonlinear 3D FE models to predict bearing capacity of PBLs. It was reported that the ultimate capacity of PBLs was barely influenced by varying the transverse steel rebar area. In order to evaluate the property of T-shaped PBLs, Vianna et al. [15] used numerical models based on ANSYS's Shell63 elements. Numerical results revealed that the ductility of PBL was significantly improved by reducing the flange plate thickness. Allahyari et al. [16] assessed the behavior of PBLs by

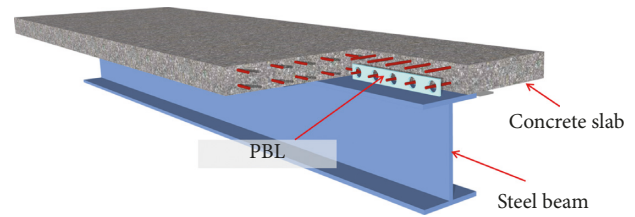


FIGURE 1: Schematics of the composite beam with PBL connectors.

employing Bayesian neural network models. They found that the shear strength of PBL was dominated by the concrete dowel's area. In addition to the use of FE simulation, experimental studies on PBL connectors and the influence of different parameters that affect its shear stiffness, strength, and load-slip response were gradually established during the past few decades or so. Empirical formulas for predicting bearing resistance of PBL fabricated with normal concrete are commonly found in the literature [17–27].

The majority of published researches in this area has focused mainly on behavior of PBLs in composite beams fabricated from normal concrete or high-strength concrete [4–27]; however, very few were related to beams made of RAC materials [18, 28]. Due to the fact that mechanical behavior of PBL varies with RAC properties, a deeper knowledge concerning mechanical behavior of PBL using RAC becomes crucial [9]. As stated earlier, the main objective of this study is to explore the structural behavior of PBL connectors embedded in the RAC slabs of composite beams. In this paper, results of an experimental program performed on the PBL are presented and discussed. An FE model of the PBL was established to get a better insight into the effects of various factors. The numerical model was verified by the experimental results, and a parametric study was performed to assess the influence of varying different parameters such as the transverse steel rebar diameter and perforated steel plate thickness and strength. It is expected that the outcomes of this study could serve as a reference for the application of PBL in RAC slabs of composite beams.

2. Push-Out Tests

2.1. Specimen Design. In this study, the standard push-out test protocol recommended by Eurocode 4 [29] for shear connectors is adopted for exploring the behavior of PBL using RAC materials. Figure 2 presents the specimen configuration layout. As shown in this figure, the push-out model consists of H-shaped steel with perforated steel plates that are vertically welded alongside the steel flanges. The perforated steel plates are embedded into the concrete slabs. Foam blocks with a thickness of 50.0 mm, which were used to eliminate the concrete end-bearing effect, were attached to the bottom of the perforated steel plates. In this arrangement, transverse steel rebar and the concrete cylinders inside the steel holes form the PBL-reinforced concrete dowel.

Figure 3 shows detailed geometric dimensions of the typical push-out specimens evaluated in this study. The concrete slab width (w_c) is 600.0 mm, with a depth (t_c) of 180.0 mm, and a height (h_c) of 330.0 mm. As shown in

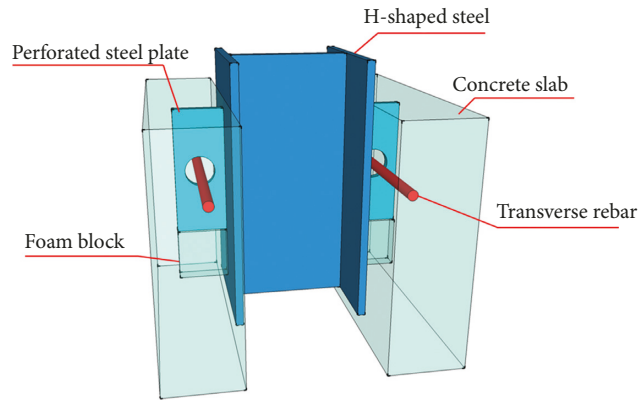


FIGURE 2: Schematics of the standard push-out specimen: (a) front view; (b) side view; (c) top view; (d) geometric dimensions of perforated steel plate. (All dimensions are in mm).

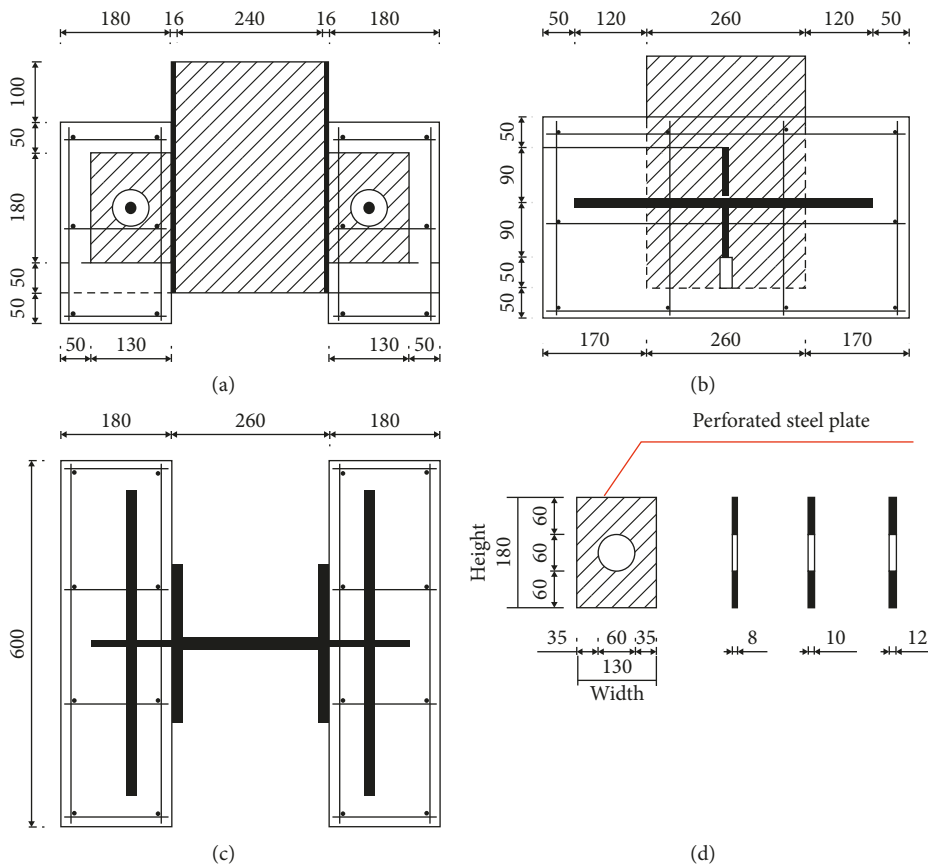


FIGURE 3: Dimensions for push-out specimens: (a) front view; (b) side view; (c) top view; (d) geometric dimensions of the perforated steel plate. (All dimensions are in mm).

Figure 3, the total height (H) of the H-shaped steel is 272.0 mm, with a steel flange total width (w_f) of 260.0 mm. The thicknesses of both steel web and flange of the H-shaped steel are 16.0 mm. The width of the perforated steel plate (w_s) is 130.0 mm, with a height (h_s) of 180.0 mm. The diameters of the circular openings, transverse steel rebars, and stirrups are 60.0 mm, 20.0 mm, and 10.0 mm, respectively. In the analysis, the thickness (t_s) of perforated steel plate was selected as the test parameter.

Table 1 summarizes the push-out specimens evaluated in this paper that consists of specimens using perforated steel plates with the following thicknesses: 8.0 mm, 10.0 mm, and 12.0 mm. In this study, six specimens in total were evaluated where two of each type were fabricated and tested. As shown in Table 1, the capital letter “R” used for specimens’ labels denotes the specimens with RAC materials, while the lowercase letter “t” and the number followed represent the perforated steel plate thickness and the corresponding

TABLE 1: Specimen characteristics.

Group	Specimen code	Thickness of the perforated steel plate (mm)	Number of holes	Diameter (mm)		
				Hole	Transverse rebar	Stirrups
1	R-t8	8				
2	R-t10	10	1	60	20	10
3	R-t12	12				

thickness value. For example, “R-t10” describes a push-out specimen that is casted using RAC materials with a 10.0 mm-thick perforated steel plate.

2.2. Specimen Fabrication and Testing. The recycled coarse aggregates employed in this study to produce the RAC were provided by a waste recycling commercial company. The measured nominal diameter of the recycled coarse aggregates was between 5.0 mm and 35.0 mm. The apparent and bulk densities of the coarse aggregates are 2,653.0 kg/m³ and 1,314.0 kg/m³, respectively. The measured water absorption percentage of coarse aggregates is 4.69%. Recycled fine aggregates were not used due to their absorption capacity, which can produce large shrinkage and permeable cement paste. The recycled coarse aggregate replacement rate for the RAC in this study was 100%. The target compressive strength of the RAC was 50.0 MPa. The compressive strength of RAC material was tested on the standard cubes with a side length of 150.0 mm. The RAC modulus of elasticity was measured via standard cylinder samples with a diameter of 150.0 mm and a height of 300.0 mm. All the cubes and cylinders were casted using the same batch of RAC that was used in fabricating the push-out specimens. The RAC was produced in an automatic mixing machine, and the mix proportions and tested material properties for the RAC are tabulated in Table 2.

The mechanical properties of the steel used in this study were conducted according to GB/T1499.2 [30]. The measured yield strength, tensile strength, and elasticity modulus of the HRB400 reinforcements were 400.0 MPa, 554.0 MPa, and 210.0 GPa, respectively. The corresponding mechanical properties of the perforated steel plate in the Q253 grade were 315.0 MPa, 403.0 MPa, and 210.0 GPa, respectively.

The push-out test protocol followed the layout described in Eurocode 4 [29], where the load was applied by a calibrated 10,000 kN hydraulic testing machine in a displacement-control regime at a rate of 0.2 mm/min. The experiment was terminated when the load in the postpeak stage dropped to 80% of the peak load, and the specimens did not fail in less than 15 minutes. Figure 4 depicts the typical push-out test setup adopted in this study. This figure shows that calibrated dial indicators were installed to acquire the vertical displacement that reflects the relative slip between the perforated steel plate and the concrete slab. Strains in the transverse steel rebars were measured using electrical strain gauges mounted along the longitudinal direction of the transverse steel rebar.

2.3. Experimental Results

2.3.1. Failure Modes. For all push-out specimens evaluated in this study, identical failure mode was observed. Figure 5

shows the typical cracking mode for RAC slabs. For the convenience of comparison, the cracking mode for PBL using normal concrete is also presented in this figure. The cracks on the surfaces of RAC slabs were initiated by the formation of cracking near the bottom region of the perforated plate and then propagated at an angle and widened as the load increased to peak. Cracked RAC on side surfaces finally spalled from the slabs (see Figure 5(b)), which was similar to the PBL embedded in normal concrete (see Figure 5(c)) [20]. Based on test observation and examination of cracking loads for different specimens, it was found that the initial cracking loads for push-out specimens with thicker perforated steel plate were relatively higher than those recorded for thinner plates. For example, the initial cracking loads for specimens R-t10 and R-t12 were 20% and 36%, respectively, which are higher than those of the R-t8 specimen with smaller thickness. This may be ascribed to the fact that the PBL with thick perforated steel plate produced lower local plastic deformation that reduced both in-plane moment and uplift force around the steel plate hole and thus delayed crack formation.

The steel elements used for fabricating the push-out specimens were taken out from the demolished concrete slabs. Figure 6 shows the typical failure pattern of perforated steel plates and transverse steel rebars. As shown in this figure, the failure of the PBL was determined by the fracture of the perforated steel plate. No apparent buckling or shearing deformations were observed in transverse steel rebars, and neither concrete dowel crushing inside the hole was witnessed. As shown in Figure 6(a), yielding of the perforated steel plates occurred at the plate opening edge, and the perforated steel plates were ruptured in the vertical direction starting from the upper region of the hole, similar to PBL fabricated using normal concrete that was previously reported by Xiao [20] and Leonhard et al. [5] (see Figure 6(d)). Due to the small thickness of the perforated steel plate, large plastic deformation was observed for specimen R-t8 steel plates that were ultimately fractured in both horizontal and vertical directions. For specimen R-t10, only vertical fracture was observed at the region adjacent to the hole upper edge. However, for specimen R-t12, cracking was developed at the welding roots, despite the vertical rupture that occurred at the upper edge of the hole section.

2.3.2. Mechanical Characterization Experimental Results.

The measured mechanical characteristic results of the PBL using RAC are summarized in Table 3. For the ease of discussion, test results for PBL using normal concrete reported by Xiao et al. [20] are also provided in Table 3. It should be noted that data presented in Table 3 are the total

TABLE 2: Mix design and material properties of RAC.

Cement	Standard sand	Mix proportions (kg/m ³)			Material properties (MPa)	
		Recycled aggregate	Water	Water reducer	Compressive strength	Elasticity modulus
485	536	1,194	185	4.85	57.1	31.0 × 10 ³

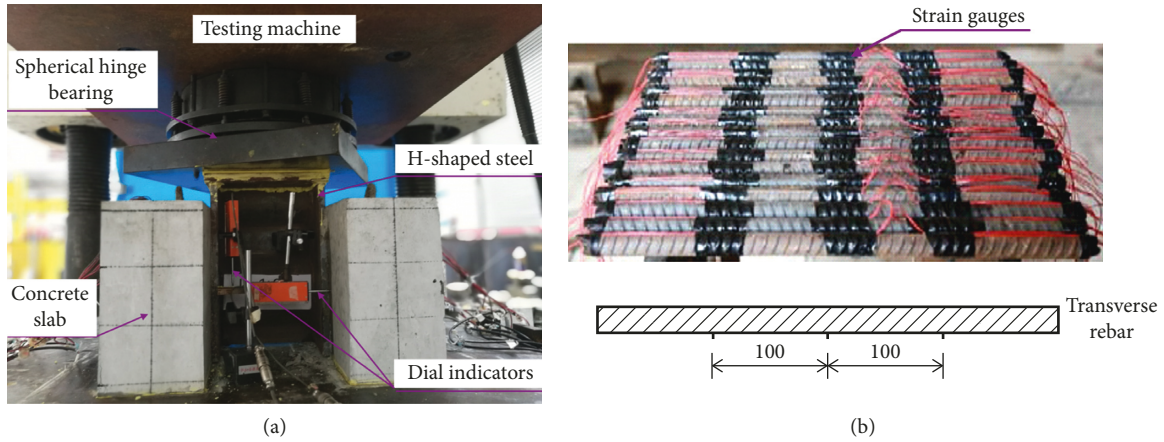


FIGURE 4: Push-out test apparatus: (a) general layout; (b) strain gauge arrangement (unit: mm).

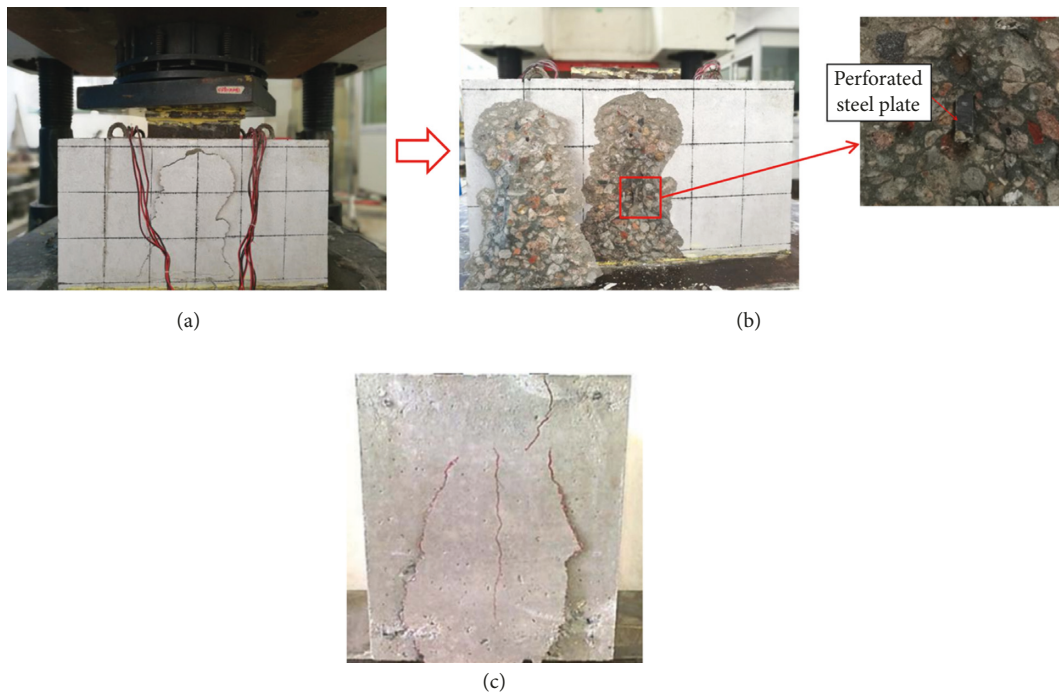


FIGURE 5: Crack distributions for push-out specimens (R-t10 example).

values of each push-out specimen that consisted of PBL connectors embedded in each concrete slab.

The shear stiffness (K_s) is defined herein as the secant stiffness at the slip of 0.2 mm, which is the maximum allowed slip at the steel-concrete interface for composite structures under the service limit state [19]. The initial cracking load (V_{cr}) is the load at the first appearance of the concrete crack. The elastic load (V_e) is the load at the end of the initial linear

behavior stage of the specimen. The ultimate shear strength (V_u) is the maximum load obtained for each specimen. The relative slip (S_u) is the slip when maximum load was achieved. The characteristic strength, V_{rk} , associating with the ultimate shear strength, V_u , is reduced by 10% in the postpeak stage. The characteristic slip (S_{rk}) refers to the slip that occurs at the characteristic strength (V_{rk}). The discussion in the following sections is related to the average

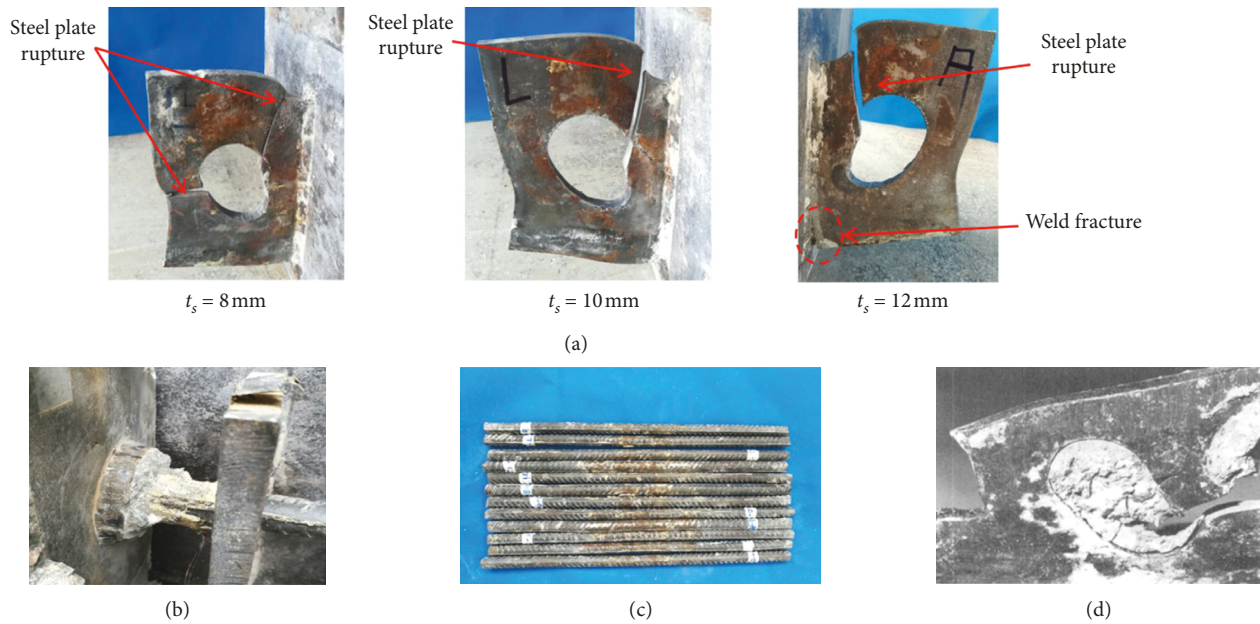


FIGURE 6: Failure patterns for components in concrete slabs: (a) perforated steel plates; (b) reinforced concrete dowel by the hole; (c) transverse steel rebars by the hole; (d) perforated steel plates for PBL using normal aggregate concrete.

TABLE 3: Push-out test summary results.

Specimen code	Elastic load (kN)		Shear stiffness (kN/mm)		Initial cracking load (kN)		Ultimate resistance (kN)		Relative slip (mm)		Characteristic resistance (kN)		Characteristic slip (mm)	
	V_e	Ave.	K_s	Ave.	V_{cr}	Ave.	V_u	Ave.	S_u	Ave.	V_{rk}	Ave.	S_{rk}	Ave.
R-t8	Spe.-1	477	2850	2786	539	552	976	986	29.28	31.55	878	838	35.66	37.19
	Spe.-2	490	2722	2786	565	552	996	986	33.82	31.55	797	838	38.72	37.19
R-t10	Spe.-1	601	3103	3185	671	664	980	1028	23.93	23.50	882	925	30.91	30.25
	Spe.-2	633	3267	3185	657	664	1075	1028	23.06	23.50	968	925	29.59	30.25
R-t12	Spe.-1	698	3932	3876	738	750	1138	1112	18.37	20.47	1024	1001	30.25	30.61
	Spe.-2	740	3819	3876	762	750	1086	1112	22.56	20.47	977	1001	30.97	30.61
PT25T [20]	361		--	--	--	--	915		20.39		824		29.68	

values since the two push-out specimens in each group give similar results.

From Table 3, one can see that both shear stiffness and ultimate strength of PBL connectors embedded in RAC increased as the perforated plate thickness increased. For example, the shear stiffness and ultimate strength of specimen R-t10 increased by 14.3% and 4.3%, respectively, as compared to the corresponding values obtained from specimen R-t8 test. The associated improvements in stiffness and strength for specimen R-t12 are 39.1% and 12.8%, respectively, as compared to those obtained from specimen R-t8 push-out test. These phenomena are expected because the use of a thicker perforated plate provided a higher load-bearing capacity and delayed the occurrence of yielding in the steel plate. With respect to observed relative slips, decrements of 18.7% and 17.7% were observed for specimens R-t10 and R-t12, respectively, as compared to those of group R-t8. The drop in the relative slip correlated well with the smaller deformation measured in the perforated steel

plate of specimens R-t10 and R-t12 (refer to Figure 6(a)). As compared to the PBL with similar geometric dimensions (perforated plate with thickness of 8.0 mm, hole diameter of 60.0 mm, and transverse rebar diameter of 25.0 mm) embedded in normal concrete [20], the shear strength of R-t8 was 7.8% higher than the normal concrete counterparts. This may be ascribed to the comparatively higher strength of the RAC and transverse rebar used in present tests. The characteristic slip for all specimens using RAC was far larger than 6.0 mm, which is the lower limit value for a ductile shear connector suggested in Eurocode 4 [27], indicating the favorable ductility of PBL using RAC in steel-concrete composite beams.

2.3.3. Load-Slip Curves. The vertical displacements of the H-shaped steel, which reflect the relative slip between the perforated steel plate and RAC slabs, were recorded during each test. Figure 7 presents the measured load-slip curves for

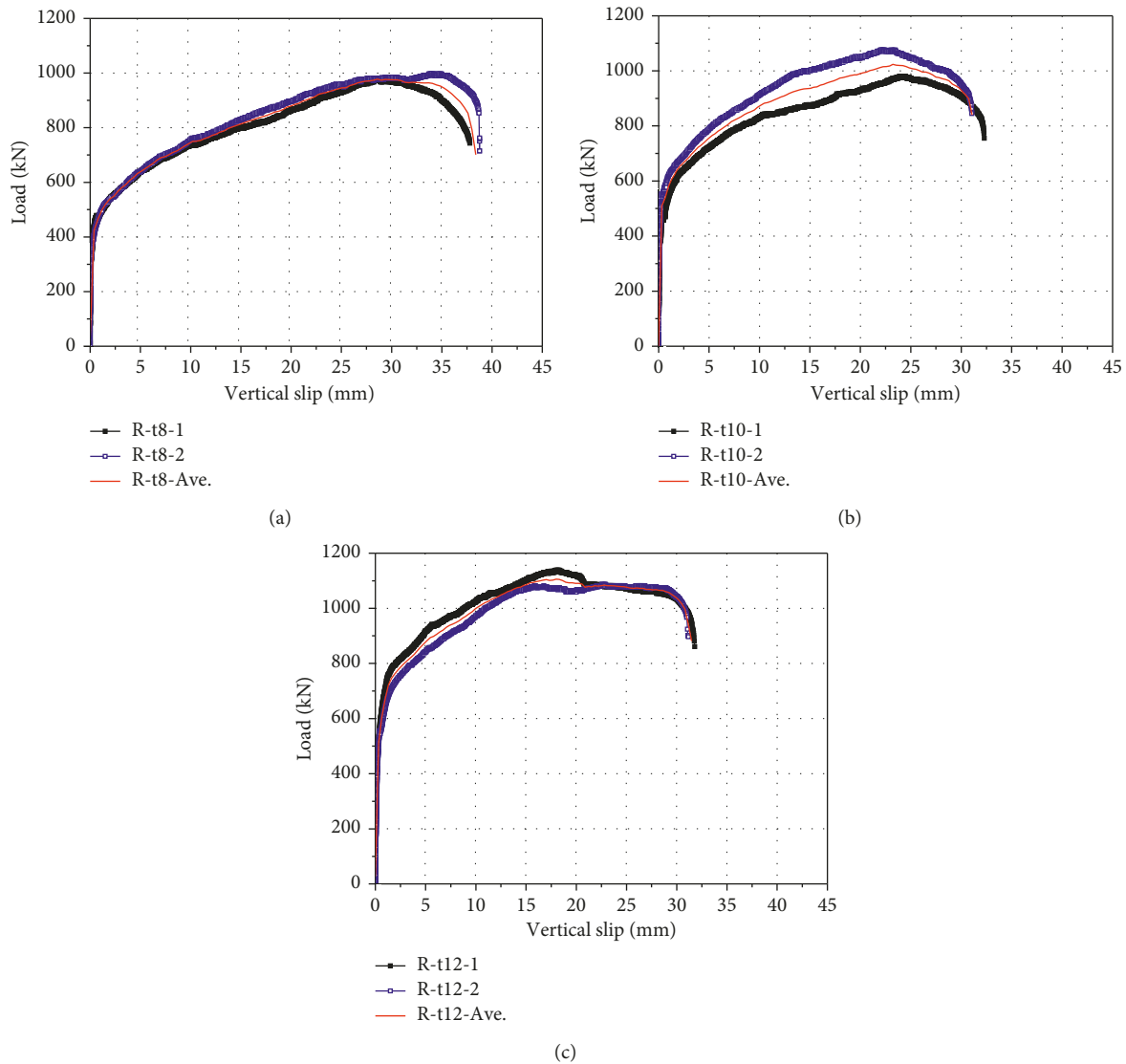


FIGURE 7: Load-slip curves: (a) group R-t8; (b) group R-t10; (c) group R-t12.

all push-out specimens. The average value of load-slip curves obtained from two identical specimens of each group is also presented. As shown in the figure, specimens using RAC from different groups exhibited similar load-slip characteristics to those of the specimens constructed using normal concrete [7]. Generally, it consists of three stages: (i) the linear elastic stage before slip reached approximately 1.0 mm; (ii) the plastic stage before load reached its peak; and (iii) the postpeak stage after PBL failure.

In the linear elastic stage, slip between the perforated steel plate and the concrete slab is small. The ascending slope of the load-slip curves is very steep, indicating the favorable initial shear stiffness of the PBL using RAC. Results also showed that the load at the end of elastic phases of the curves increased as the thickness of the perforated steel plate increased. For example, the elastic loads identified from the load-slip curves of groups R-t10 and R-t12 are 27.5% and 48.5%, respectively, which are higher than the corresponding loads obtained from R-t8 specimen test. Again, this is

expected since the PBL elastic phase was terminated once the perforated steel plate yielded, and the use of a thicker perforated steel plate provided higher stiffness. As compared to the normal concrete counterparts (perforated plate with thickness of 8.0 mm, hole diameter of 60.0 mm, and transverse rebar diameter of 25.0 mm) reported by Xiao [20], since the smaller transverse rebar used in R-t8 reserved larger space in the hole for coarse aggregates to enter, R-t8 gave 1.34 times higher elastic loads than those of the normal concrete connector. In this linear elastic stage, the adhesion-friction effects at the steel/concrete contacting surfaces resisted the applied push-out load and enhanced the stiffness of the connector.

During the plastic stage, the slip between the perforate steel plate and the concrete slab increased rapidly while the push load rate decreases. The peak load was achieved once the perforated steel plate fractured. As shown in Figure 7, group R-t8 specimens exhibited a gentler slope as compared to those of R-t10 and R-12 specimens, demonstrating the

lower plastic stiffness of specimen R-t8. This also correlates well with the largest plastic deformation that was measured in the perforated steel plate of specimen R-t8 among the three groups. As the chemical adhesion effects at the interface between the perforated steel plate and concrete slabs diminish, the load applied to the specimen in the plastic stage was primarily carried by the reinforced concrete dowel inside the hole.

In the postpeak stage of the load-slip curves, the slip between the perforated steel plate and the concrete slab increases rapidly whilst the push load shows a continual decrement. From Figure 7, one can notice that providing a thicker perforated steel plate results in an increase in the peak load, while PBL relative slip decreases. Referring to Figures 7(a) and 7(b), a sharp load drop is shown once specimens reached their peak. On the other hand, a steady plateau is observed after reaching the peak load for group R-t12 (see Figure 7(c)). The differences may be attributed to the following reasons: for specimens R-t8 and R-t10, the fracture of the perforated steel plate and the achievement of peak loads occurred simultaneously, which are evidenced by the sharp drop in load on their load-slip curves; for specimens R-t12, peak load was reached prior to the total fracture of the perforated steel plate and welding roots. The stable residual load in the postpeak stage for R-t12 resulted from the torn of welding roots.

3. Parametric Investigation by Finite Element (FE) Models

3.1. FE Element Selection. Commercial finite element package ABAQUS was used for numerical analysis of the push-out test. In the FE model, the push-out specimens were simulated to validate the numerical model. The main components in the push-out specimen consisted of a perforated steel plate, concrete slab, concrete dowel, transverse rebar, and stirrups. Figure 8 shows the FE model of the specimen. Half of the real experimentally investigated push-out specimen was assumed as vertical symmetry. The main components were modeled by using eight-node solid elements (C3D8R) to achieve proper behavior of the specimen [31], while the stirrups in concrete slabs were simulated by using beam elements embedded into concrete. To ensure the accuracy and computational efficiency, a mesh sensitivity analysis was conducted. The results indicate that a denser element size of 10.0 mm for the seed edges among the perforated steel plate opening, concrete dowel, and transverse rebar and a coarse mesh size of 20.0 mm for the other part of the model provided a good compromise. Displacement-controlled failure loading was applied at a reference point at the top of the steel profile.

The surface-to-surface contact was applied to the steel and concrete interfaces to define the interaction between the components. The bottom surface of the concrete slab was restrained against the degree of freedom in the Y -direction (refer to Figure 8(a)). The symmetry boundary condition was applied to the symmetric plane of the push-out model, which means all nodes located at the symmetric plane were prevented from translating in the Z -direction and rotating in

X - and Y - directions. The surfaces of the concrete dowel contacting with the perforated steel opening were considered in the form of tie together. Now, by tying the nodes, the contacted elements would share all degrees of freedom to each other. The contact of the perforated steel plate and the concrete slab can be simulated through the contact friction elements (contact). The tangential friction coefficient between the steel plate and concrete was set as 0.6 [32]. The nominal direction was defined as hard contact but free to depart. The Abaqus/standard analysis was employed for all push-out models.

3.2. Material Modeling

3.2.1. Material Model for RAC. Concrete damage plasticity is implemented in the FE models. The stiffness degradation of concrete was defined by preset damage variables, and the failure of concrete was identified via the maximum strain in the poststage. Generally, the concrete failure mechanism includes tensile cracking and compressive crushing. The evolution of the yield surface is determined by two hardening variables, which cause failure under tensile as well as compressive loading. Postfailure behavior under compression is defined by a softening stress-strain response. The strain-softening behavior of cracked concrete in tension is specified by tension stiffening in terms of either postfailure stress-strain behavior in tension or fracture energy cracking criterion.

Existing studies have indicated that the stress-strain constitutive model for RAC and normal concrete is very similar [2]. Accordingly, the measured RAC material properties obtained in the present experimental work were used in FE analysis, and the input stress-strain relation for RAC under uniaxial compression and tension used in the current FE analysis was determined from equations (1)–(4), which are given by [33] for normal concrete. The schematic diagram of the stress-strain relation for nonlinear structural analysis of RAC is shown in Figure 9.

The compressive stress-strain constitutive model for RAC is defined by the following equations:

For $0 \leq \varepsilon_c < \varepsilon_0$,

$$\frac{\sigma_c}{f_{cu}} = a \frac{\varepsilon_c}{\varepsilon_0} + (3 - 2a) \left(\frac{\varepsilon_c}{\varepsilon_0} \right)^2 + (a - 2) \left(\frac{\varepsilon_c}{\varepsilon_0} \right)^3. \quad (1)$$

For $\varepsilon_0 \leq \varepsilon_c$,

$$\frac{\sigma_c}{f_{cu}} = \frac{\varepsilon_c \cdot \varepsilon_0}{b(\varepsilon_c - \varepsilon_0)^2 + \varepsilon_c \cdot \varepsilon_0}, \quad (2)$$

where σ_c = compressive stress (MPa); f_{cu} = cubic compressive strength (MPa); ε_c = compressive strain at σ_c ; ε_0 = compressive strain at f_{cu} ; and a , b = coefficients for determining the ascending and descending phrases of the stress-strain curve.

Using equations (1) and (2) and the experimental material property results, the value of $a = 1.9$ and $b = 2.1$ is obtained.

The tensile stress-strain constitutive model of RAC could be defined as

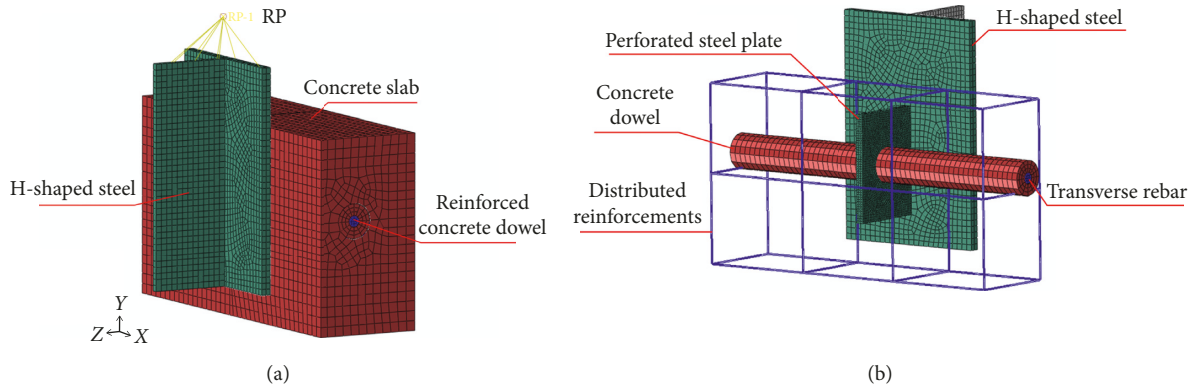


FIGURE 8: FE model: (a) half of the push-out specimen; (b) components.

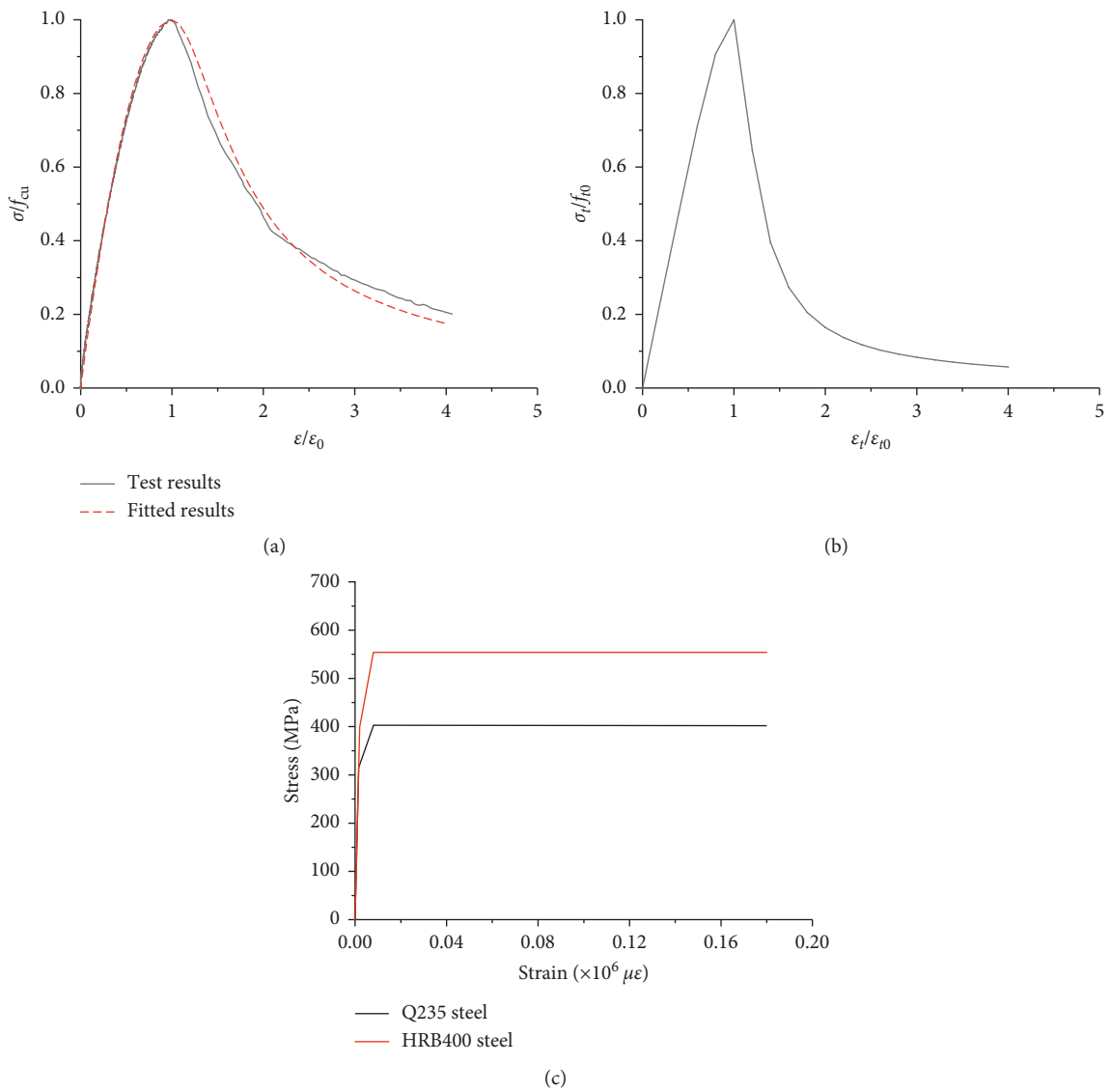


FIGURE 9: Stress-strain relationship for the materials: (a) regression of nondimensional measured compressive stress-strain relationship of RAC; (b) normalized tensile stress-strain relationship for RAC; (c) stress-strain relationship for steel components.

For $0 \leq \varepsilon_t < \varepsilon_{t0}$,

$$\frac{\sigma_t}{f_{t0}} = 1.2 \frac{\varepsilon_t}{\varepsilon_{t0}} - 0.2 \left(\frac{\varepsilon_t}{\varepsilon_{t0}} \right)^6 \quad (3)$$

For $\varepsilon_{t0} \leq \varepsilon_t$,

$$\frac{\sigma_t}{f_{t0}} = \frac{\varepsilon_t/\varepsilon_{t0}}{0.312 f_{t0}^2 ((\varepsilon_t/\varepsilon_{t0}) - 1)^{1.7} + (\varepsilon_t/\varepsilon_{t0})} \quad (4)$$

where σ_t = tensile stress (MPa); f_{t0} = characteristic tensile strength, taken as $0.1 f_{cu}$; ε_t = tensile strain at σ_t , $\varepsilon_t = \sigma_t/E_c$; ε_{t0} = ultimate tensile strain, assumed to be 0.001 when lacking of test results; and E_c = modulus of elasticity.

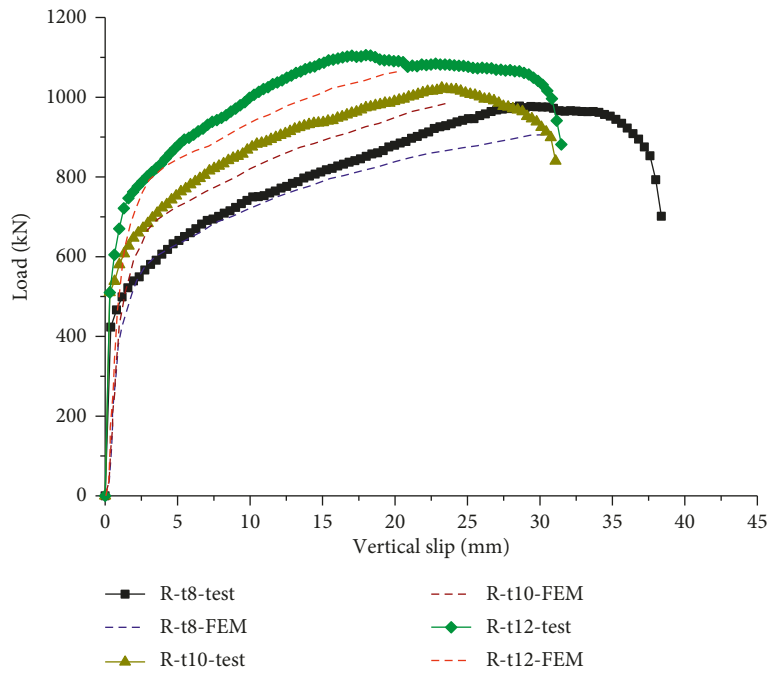
3.2.2. Material Model for Steel. For perforated steel plate and transverse rebars, the elastoplastic model was used, and the ductile damage and fracture strain were utilized to determine the steel fracture. Similar stress-strain relationship was adopted for the transverse rebar and perforated steel plate, and their compression and tension stress-strain curve were consistent. Figure 9(c) shows the stress-strain relationship adopted for the steel. The steel components behaved as linear elastic material until yielding, followed by a plastic behavior. The modulus of elasticity for the transverse rebar and the steel plate from material tests was used as the input to the FE model as presented in Section 2.2. The density of all steel components was taken as $7,800 \text{ kg/m}^3$.

3.3. Validation of the FE Model. The load-slip curves for the test specimens were obtained by FE models. Figure 10(a) shows the comparison between the test and simulated results. Due to the comprehensive mechanism of the connector in the postfailure stage, Figure 10 only presents the initial part (up to peak load) of the predicted load-slip curves for the specimens. Acceptable accuracy is observed between the FE model and the test data, especially good prediction of ascending branch of the load-slip curves is achieved. The predicted initial stiffness of the connector, reflecting on the initial slope of the numerical load-slip curves, is slightly below the experimental curve. This may be ascribed to the variability of the concrete material properties. Figure 10(b) presents a comparison between the predicted failure pattern and test failure of the perforated steel plate. As shown in the figure, the numerical model shows good agreement with the test results. Domain failure mode of considered FE models of PBL is failure of the perforated steel plate, considering global failure of the concrete slab and shear failure of the concrete dowels. The ultimate loads are similar and present a conservative trend compared to the experimental results. Specifically, the average ratio between the numerical results and the experimental ultimate resistance is 0.95. From the view of design safety, the FE model shows good agreement with the experimental results. Considering the variability of the real materials, the nominal value used in the FE model is considered sufficient valid.

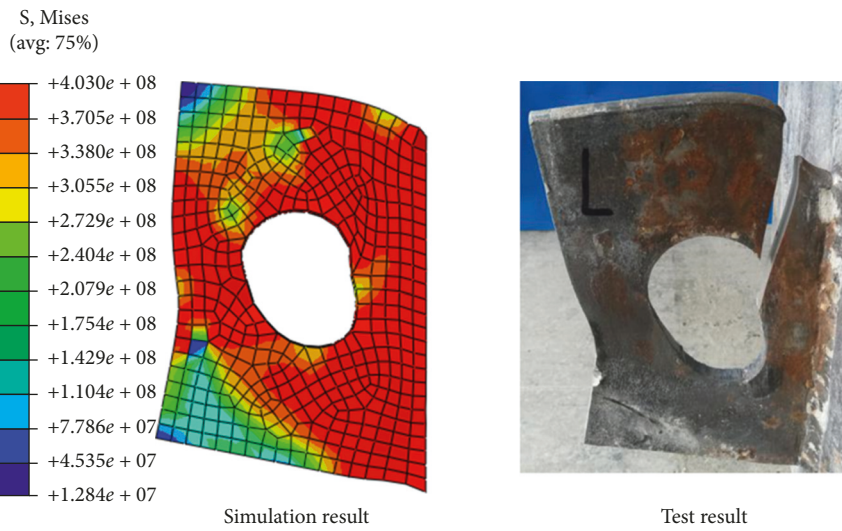
3.4. Influence of Perforated Steel Plate Thickness. The domain failure pattern of the PBL tested in the current study is the fracture of the perforated steel plate. In order to further examine the performance of the PBL with thicker perforated steel plate, an extensive numerical investigation by varying the plate thickness is performed herein. Figure 11 shows the initial phase (up to peak load) of the load-slip curves for the PBL predicted by the FE models. It appears that, by increasing the thickness of the perforated steel plate from 12.0 mm to 24.0 mm, the initial stiffness was barely increased, whereas the ultimate resistance showed a continual increase as the plate thickness increases. Specifically, the ultimate resistance of the PBL with a thickness of 16.0 mm, 20.0 mm, and 24.0 mm increased by 16.5%, 25.2%, and 25.7%, respectively, in comparison with that with the 12.0 mm-thick perforated steel plate. It is noted that the resistance of PBL increased until the thickness reaches 20 mm, and the further increase of the thickness hardly affects the shear capacity. Concerning to the failure modes, as can be seen in Figure 12, the PBL with a thickness below 20.0 mm failed due to the fracture of the perforated steel plate and then alternated to rupture of the transverse rebar or cracking of the concrete slabs after thickness exceeding 20.0 mm. From the view of fully utilizing the component strength, for PBL having a hole diameter of 60.0 mm and a rebar diameter of 20.0 mm, the favorable thickness of the perforated steel plate in the Q235 steel grade is 20.0 mm.

3.5. Influence of Perforated Steel Plate Strength. Despite the thickness of the perforated steel plate, the strength of the steel plate also significantly affects the performance of the connector. The structural steel in China Code [30] consists of Q235, Q345, Q390, Q420, and Q460, of which the number after Q represents the nominal yield strength of the steel. Figures 13 and 14 present the initial part of predicted load-slip curves and failure pattern for the PBL with different steel strengths, respectively. All the load-slip curves give similar initial ascending slope, indicating that the initial stiffness of the PBLs casted with RAC was barely affected by the plate strength. Concerning to the ultimate resistance, it is observed that the PBL using the high-grade steel plate presents large ultimate resistance before the yield strength exceeds 390 MPa. Specifically, comparing to the PBL using Q235 grade steel, the resistance of PBL using Q345 and Q390 increased by 14.3% and 18.4%, respectively. After the strength exceeds 390.0 MPa, the ultimate resistance of the PBL almost remains constant as the strength continuously increases. Referring to Figure 14, at the ultimate state of the PBL using steel grade Q390, the plastic deformation in the perforated steel plate is small, whereas the bending deformation in the transverse rebar becomes significant. The alternated failure modes of the PBL suggest that Q390 steel could preferably utilize the capacity of the PBL with the dimensions in the present study.

3.6. Influence of Transverse Rebar Diameter. Previous studies revealed that the diameter of the transverse rebar passing



(a)



(b)

FIGURE 10: Validation of the FE models: (a) load-slip curves; (b) failure modes of the perforated steel plate (group R-t10 example).

through the hole is critical for a PBL. In this simulating work, the rebar diameters are selected as 20.0 mm, 16.0 mm, 12.0 mm, 8.0 mm, and 0.0 mm. Figure 15 shows the load-slip curves predicted by the FE models. Similar to the connector fabricated using plain concrete, FE numerical results confirmed the higher initial stiffness, larger elasticity, and ultimate resistances of PBL having larger diameter of rebar, in comparison to those with comparatively small steel rebar. Table 4 summarizes the numerical results of the PBL. From this table, one can see that the elastic resistance of the PBL increased by 25.0% as the diameter increased from 8.0 mm to 20.0 mm and that the ultimate strength of connectors with rebar diameters of 8.0 mm, 12.0 mm, 16.0 mm, and 20.0 mm

increased by 15.7%, 33.9%, 42.8%, and 43.9%, respectively, as compared to those without the rebar. By comparing the predicted results of groups R-t12-Q235-d16 and R-t12-Q235-d20, it was shown that providing a transverse rebar of 20.0 mm in diameter only limitedly increases the elasticity resistance and the ultimate resistance of the PBL, as compared to those with a rebar of 16.0 mm in diameter. By checking their failure modes, it is found that the PBL with the diameter of transverse rebar smaller than 16.0 mm failed due to rebar fracture, whereas failure of the PBL using transverse rebars larger than 20.0 mm in diameter alternates to the fracture of the perforated steel plate or cracking of concrete slabs.

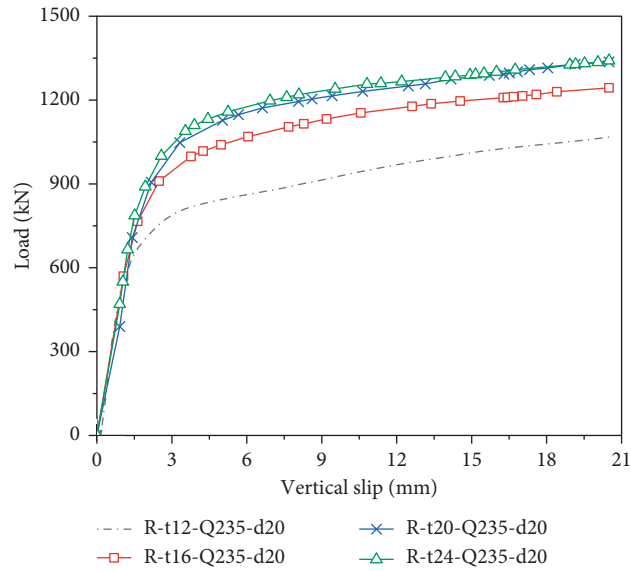


FIGURE 11: Load-slip curves for PBL with different plate thicknesses.

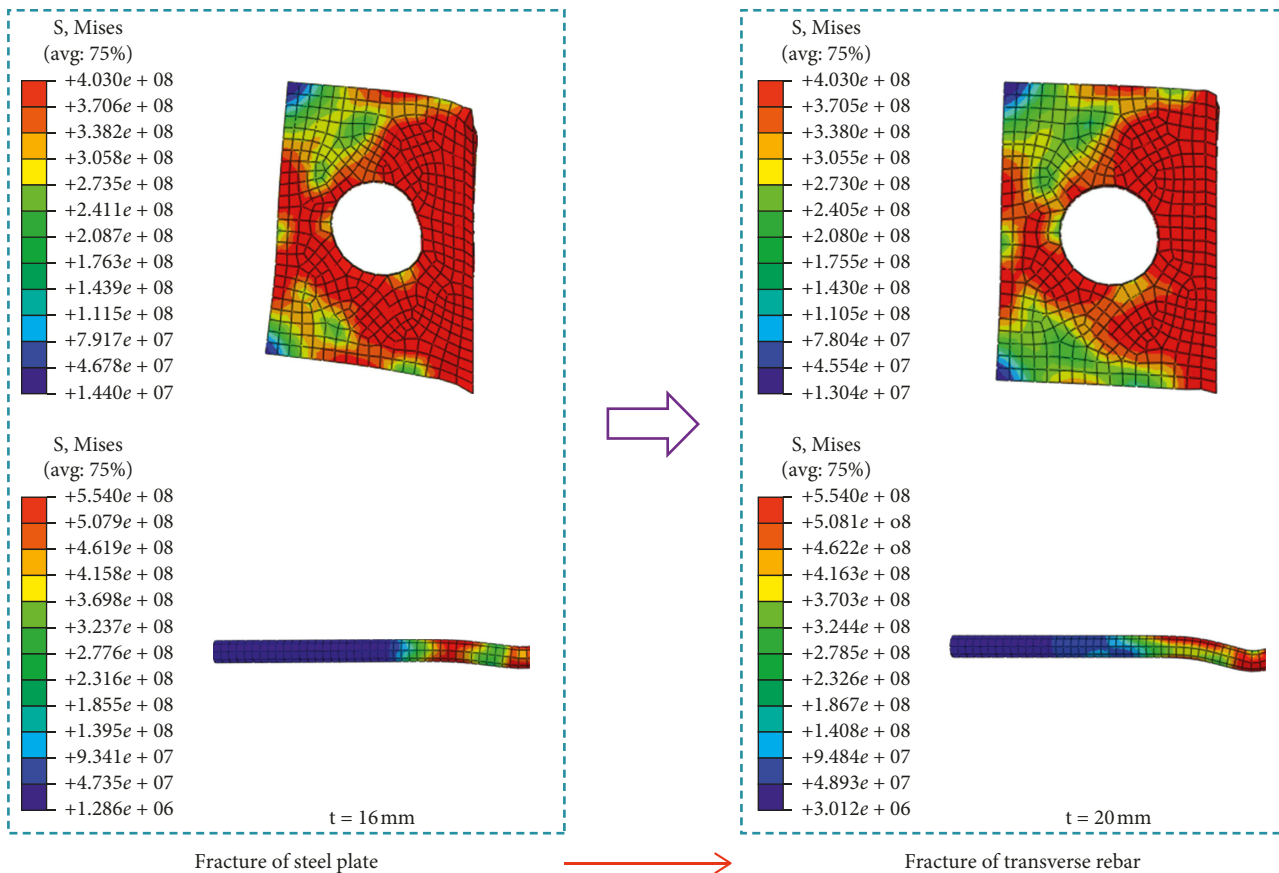


FIGURE 12: Failure patterns for PBL with different plate thicknesses.

4. Evaluation of Existing Formulations on PBL Using RAC

Various formulas for predicting the shear resistance of PBL embedded in normal concrete have been proposed recently

[22–27]. The majority of these equations comprises four terms: bond effects at the steel plate-concrete interface, transverse rebar resistance, concrete dowel resistance, and the end-bearing resistance. Equations (5) through (10) are expressions for several typical equations.

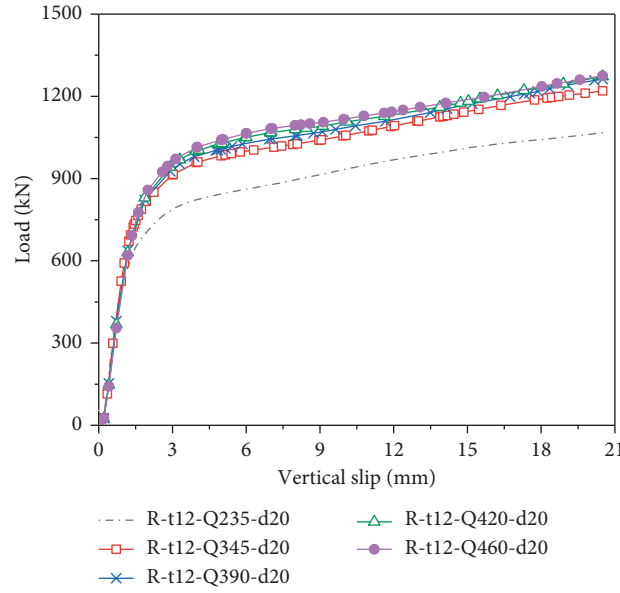


FIGURE 13: Load-slip curves for PBL with different steel strengths.

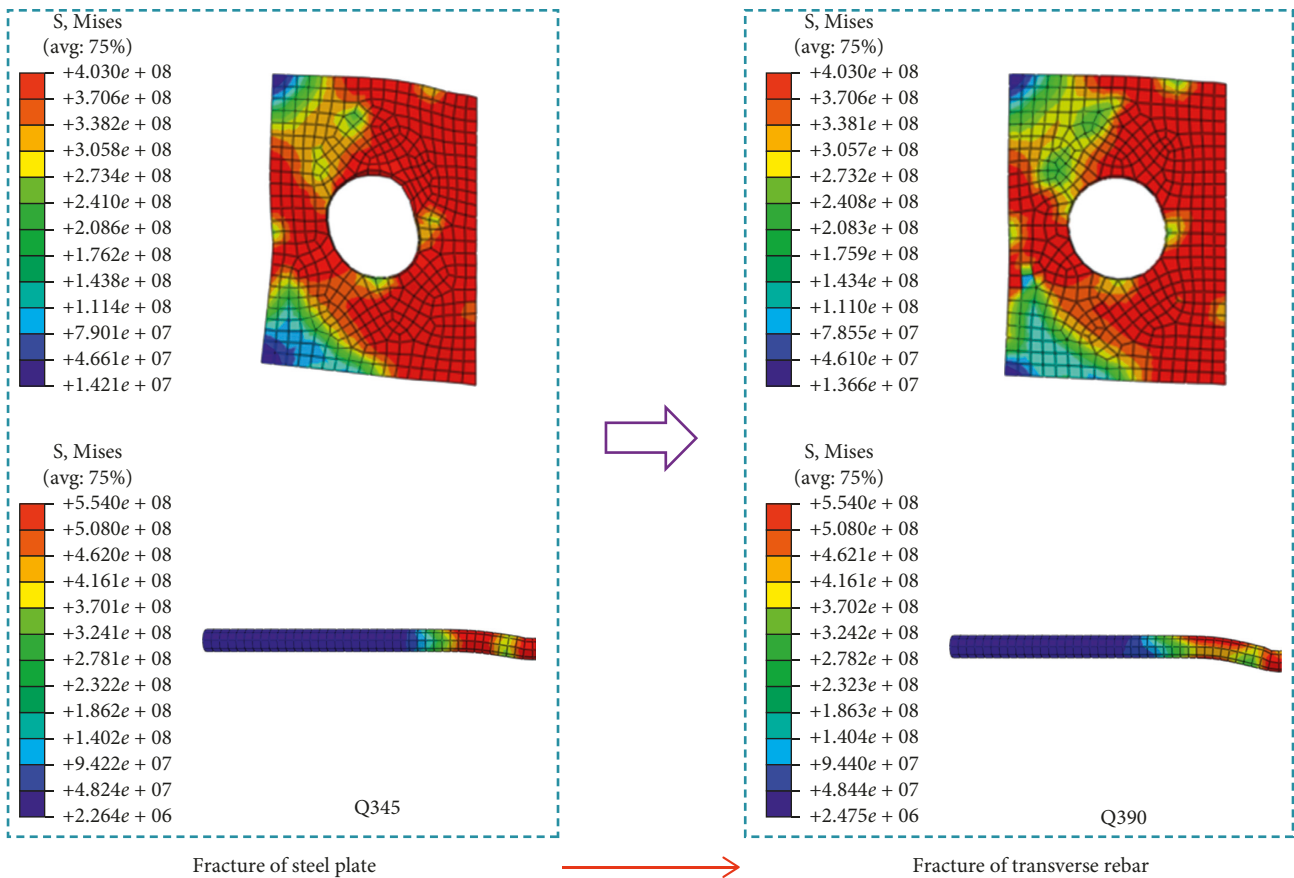


FIGURE 14: Failure patterns for PBL with different steel strengths.

The analytical model proposed by Yang and Chen [22], which describes the shear resistance of PBL by considering the factors of end-bearing effect, hole number, and rebar diameter, is as the following:

$$V_u = 5.15A_e f_{cu} + 5.41A_c f_{cu}^{0.57} + 2.24A_s f_y, \quad (5)$$

where A_e = area of the end-bearing zone (mm^2); f_{cu} = cubic compressive strength of the concrete (MPa); A_c = sectional

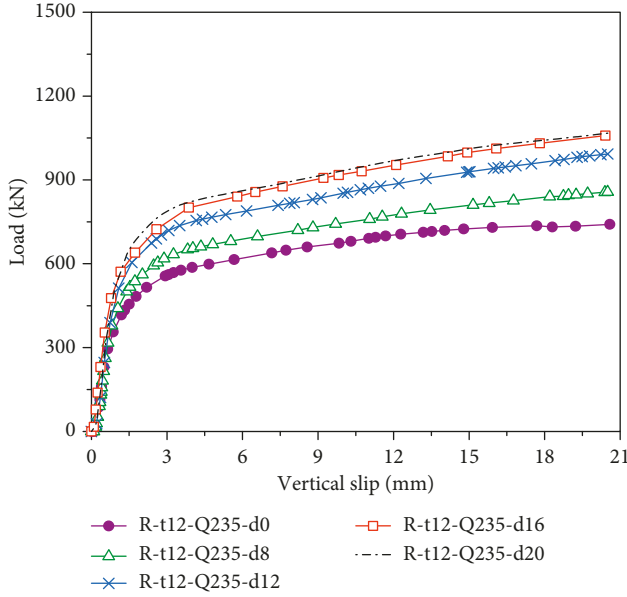


FIGURE 15: Load-slip curves for PBL with different rebar diameters.

TABLE 4: Influence of the transverse rebar diameter.

Specimen	Rebar diameter (mm)	Shear stiffness (kN/mm)	Elasticity resistance (kN)	Ultimate resistance (kN)
R-t12-Q235-d0	0	2,358	454	741
R-t12-Q235-d8	8	2,547	515	857
R-t12-Q235-d12	12	2,784	602	992
R-t12-Q235-d16	16	3,036	637	1,058
R-t12-Q235-d20	20	3,182	644	1,067

area of the concrete dowel (mm^2); f_y = yield strength of the transverse rebar (MPa); and A_s = sectional area of the transverse steel rebar (mm^2).

Zhu and Wang [23] conducted 33 push-out tests to evaluate the structural behavior of PBL fabricated using normal concrete. Based on the experimental results, the following equations for predicting the ultimate resistance of PBL were established:

$$V_u = \beta_1 k_a \left(\frac{t_s}{D} \right)^{1/2} n D^2 \sqrt{f_{ck}} + \beta_2 b_f L_c + \beta_3 A_s f_y, \quad (6)$$

where k_a = coefficient affecting the concrete strength, taken as 1.0 for the case without transverse pretension and in other cases, taken as 0.9; β_1 , β_2 , and β_3 = regression factors, normally taken as 1.972, 3.417, and 1.334, respectively; t_s = thickness of the perforated steel plate (mm); V_u = ultimate resistance of the PBL (N); D = diameter of the hole in the perforated steel plate (mm); n = number of the hole; f_{ck} = compressive strength of the concrete (MPa); b_f = width of the steel flange (mm); and L_c = length of the

contacting area between the steel flange and the concrete slab (mm).

Based on the experimental and numerical results from 24 push-out specimens, the following equations were proposed to calculate the capacity of PBL embedded in normal concrete slabs by Wang et al. [24]:

$$V_u = 0.498 A_c \sqrt{f_c} + 0.255 A_s f_y + 0.065 A_{tr} f_s, \quad (7)$$

where A_{tr} = area of the steel stirrups in concrete slabs (mm^2); f_c = cylinder compressive strength of the concrete (MPa); and f_s = yield strength of the steel stirrups (MPa).

Equation (8) describes the formula that was developed by Jiang and Wang [25] for evaluating shear resistance of PBL using normal virgin concrete:

$$V_u = 1.8 \sqrt{f_c} A_c^{0.4} + 0.8 A_s f_y. \quad (8)$$

Di et al. [26] investigated the influence of the diameter and shape of the hole on structural behavior of PBL through 39 push-out specimens, and the following equations were proposed based on the analytical results.

For the PBL with the transverse steel rebar:

$$V_u = 1.23 A_c^{0.85} f_{cu} \lambda^{0.22} t^{0.45} + 1.64 A_s f_y. \quad (9A)$$

For the PBL without the transverse steel rebar:

$$V_u = 1.4 A_c^{0.85} f_{cu} \lambda^{0.22} t^{0.45}, \quad (9B)$$

where λ = coefficient for the transverse restraint from the concrete block, $\lambda = (A_{tr} f_y + A'_s f'_s) / A_c f_{cu}$; A'_s = sectional area of the steel plate that acts as the transverse confinement (mm^2); and f'_s = yield strength of the steel plate (MPa).

Zheng et al. [27] proposed equation (10) to predict the shear capacity of PBL using normal concrete:

$$V_u = 1.76 \alpha_A (A - A_s) f_c + 1.58 A_s f_y, \quad (10)$$

where α_A = effective shear area ratio of the concrete dowel per hole, $\alpha_A = 3.80 (A_s / A)^{2/3}$; and A = area of the hole (mm^2).

Using the above set of equations, the predicted shear resistances for the PBL tested and simulated in the current study are obtained. Table 5 presents the related results.

As can be seen in Table 5, large discreteness in the predicted shear resistance was observed for all equations. The above formulas were developed based on the regression of experimental results from push-out tests on PBL fabricated using normal concrete. All the equations exhibit conservative predictions for the PBL using RAC, except equation (5). The unsafe predicting results given by equation (5) may be ascribed to the fact that this equation comprised the resistance provided by end-bearing concrete, which was eliminated in the current push-out specimens. Using equations (6) through (10), average $V_u^{\text{Test}} / V_u^{\text{Pre}}$ ratios between 1.43 and 2.11 are calculated. These equations are proposed based on experimental results achieved from push-out tests, of which the dominant failure pattern was fracture of the reinforced concrete dowel by the hole. In contrast, the failure of PBL using RAC tested and simulated in this study was dominated by the fracture of the perforated steel plate, which

TABLE 5: Comparisons between experimental and predicted resistances.

Specimen	Shear resistance per PBL							Test (FE)	Test (FE)					
	Test (FE)	Eq. (5)	Eq. (6)	Eq. (7)	Eq. (8)	Eq. (9A) and (9B)	Eq. (10)	Eq. (5)	Eq. (6)	Eq. (7)	Eq. (8)	Eq. (9A) and (9B)	Eq. (10)	
Test	R-t8-d20	493	723	386	491	384	339	382	0.68	1.28	1.00	1.28	1.45	1.29
	R-t10-d20	514	800	402	491	384	353	382	0.64	1.28	1.05	1.34	1.46	1.35
	R-t12-d20	556	877	417	491	384	366	382	0.63	1.33	1.13	1.45	1.52	1.46
FE	R-t16-d20	648	1,029	443	491	384	388	382	0.63	1.46	1.32	1.69	1.67	1.70
	R-t20-d20	696	1,183	467	491	384	407	382	0.59	1.49	1.42	1.81	1.71	1.82
	R-t24-d20	699	1,206	488	491	384	424	382	0.58	1.43	1.42	1.82	1.65	1.83
	R-t12-d0	371	612	—	183	298	196	—	0.61	—	2.03	1.24	1.89	—
	R-t12-d8	429	655	278	232	311	207	92	0.65	1.54	1.85	1.38	2.07	4.66
	R-t12-d12	496	707	310	294	329	245	172	0.70	1.60	1.69	1.51	2.02	2.88
	R-t12-d16	529	781	357	380	353	298	270	0.68	1.48	1.39	1.50	1.78	1.96
	Average								0.64	1.43	1.43	1.50	1.72	2.11

is significantly different from the previous published push-out test results. Consequently, the strength of PBL embedded in RAC with that is dominated by the failure of perforated steel plate fracture cannot be well predicted by the existing formulas established for PBL using normal concrete with the dowel fracture-dominated failure mode.

As stated earlier, the main objective of this study is to investigate the structural behavior of PBL fabricated with the RAC in steel-concrete composite beams using limited number of push-out specimens and FE models. For this reason, it is highly recommended that more experiments be performed in order to develop reliable formula for the PBL using RAC in steel-concrete composite beams.

5. Conclusion

In this study, the results of an investigation on predicting structural behavior of PBL fabricated using RAC by six push-out specimens are presented and discussed. A numerical model is developed to simulate the behavior of the PBL using RAC. This model is used to evaluate the effects of an expanded range of the design variables including the diameter of the transverse rebar and perforated steel plate strength and thickness. Based on the results of this investigation, the following conclusions are drawn:

- (1) The perforated steel plate with larger thickness provides higher shear resistance; however, it reduces the slip capacity of PBL using RAC. For example, experimental results indicate that the ultimate strength of PBL with a plate thickness of 10.0 mm and 12.0 mm increased by 4.3% and 12.8%, respectively, as compared to a steel plate with 8.0 mm thickness. The PBL using RAC exhibits sufficient ductility to ensure the composite action between the steel and concrete members.
- (2) The PBL shear strength increases as the perforated steel plate strength increases. For example, as compared to the PBL fabricated from Q235 grade steel, the resistance of PBL fabricated from both Q345 and Q390 steel grades increased by 14.3% and

18.4%, respectively. Due to the ultimate state change of PBL, the increasing rate of shear strength decreased as the steel grade increased from grade Q390 to grade Q460.

- (3) The use of the transverse steel rebar with a larger diameter contributes to higher PBL initial stiffness, larger elasticity, and ultimate strength. For example, as the diameter increased from 8.0 mm to 20.0 mm, the stiffness and the ultimate strength of the PBL increased by 25.0% and 43.9%, respectively. A further increase in the steel rebar diameter led to the PBL failure mode change from fracture of the steel plate to a dowel rupture.
- (4) Results also indicated that the shear strength of PBL connectors embedded in RAC materials that are determined by steel plate fracture is difficult to be precisely predicted using existing equations that are developed based on the dowel fracture failure mode. In order to develop reliable expressions for predicting the strength of PBL connectors embedded in RAC slabs, a more detailed investigation on PBL design variables is recommended.

Data Availability

All data used during the study appear in the submitted article.

Conflicts of Interest

The authors declare that they have no conflicts of interest.

Acknowledgments

The authors would like to thank the financial support provided by the National Natural Science Foundation of China (no. 51908138) and the Department of Education of Guangdong Province (no. 2018KQNCX071), and the Civil and Environmental Engineering Department at the University of California, Irvine, USA, is also acknowledged.

References

- [1] Technical Assistance Consultant's Report, "People's Republic of China: Construction and Demolition Waste Management and Recycling," vol. 68, AECOM Asia Company Limited for the PRC Ministry of Housing and Urban-Rural Development and the Asian Development Bank, Beijing, China, 2018.
- [2] M. Etxeberria, A. R. Mari, and E. Vázquez, "Recycled aggregate concrete as structural material," *Materials and Structures*, vol. 40, no. 5, pp. 529–541, 2007.
- [3] J. Xiao, W. Li, Y. Fan, and X. Huang, "An overview of study on recycled aggregate concrete in China (1996–2011)," *Construction and Building Materials*, vol. 31, pp. 364–383, 2012.
- [4] S. N. H. Ali, S. Ramli, S. Meldi, and S. Mahdi, "Various types of shear connectors in composite structures: a review," *International Journal of Physical Sciences*, vol. 7, no. 22, pp. 2876–2890, 2012.
- [5] F. Leonhard, W. Andra, H. P. Andra, and W. Harre, "New improved bonding means for composite load bearing structures with high fatigue strength," *Beton Stahlbetonbau*, vol. 82, no. 12, pp. 325–331, 1987.
- [6] W. Deng, J. Gu, and D. Liu, "Study of single perfobond rib with head stud shear connectors for a composite structure," *Magazine of Concrete Research*, vol. 5, pp. 1–15, 2018.
- [7] S. He, Z. Fang, Y. Fang, M. Liu, L. Liu, and A. S. Mosallam, "Experimental study on perfobond strip connector in steel-concrete joints of hybrid bridges," *Journal of Constructional Steel Research*, vol. 118, pp. 169–179, 2016.
- [8] S. He, Z. Fang, and A. S. Mosallam, "Push-out tests for perfobond strip connectors with UHPC grout in the joints of steel-concrete hybrid bridge girders," *Engineering Structures*, vol. 135, pp. 177–190, 2017.
- [9] C. Zhao, Z. Li, K. Deng, and W. Wang, "Experimental investigation on the bearing mechanism of perfobond rib shear connectors," *Engineering Structures*, vol. 159, pp. 172–184, 2018.
- [10] Q. Su, G. Yang, and M. Bradford, "Bearing capacity of perfobond rib shear connectors in composite girder bridges," *Journal of Bridge Engineering*, vol. 21, no. 4, Article ID 06015009, 2016.
- [11] Y. Yang and Y. Chen, "Experimental study on mechanical behavior of PBL shear connectors," *Journal of Bridge Engineering*, vol. 23, no. 9, Article ID 04018062, 2018.
- [12] D. Kraus and O. Wurzer, "Nonlinear finite-element analysis of concrete dowels," *Computers & Structures*, vol. 64, no. 5–6, pp. 1271–1279, 1997.
- [13] E. C. Ogujiofor and M. U. Hosain, "Numerical analysis of push-out specimens with perfobond rib connectors," *Computers and Structures*, vol. 62, no. 4, pp. 617–624, 1997.
- [14] S. Y. K. Al-Darzi, A. R. Chen, and Y. Q. Liu, "Finite element simulation and parametric studies of perfobond rib connector," *American Journal of Applied Sciences*, vol. 4, no. 3, pp. 122–127, 2007.
- [15] J. D. C. Vianna, S. A. L. de Andrade, P. C. G. D. S. Vellasco, and L. F. D. C. Neves, "A parametric analysis of composite beams with t -perfobond shear connectors," in *Proceedings of the SDSS' Rio 2010 Stability and Ductility of Steel Structures*, pp. 8–10, Rio de Janeiro, Brazil, September 2010.
- [16] H. Allahyari, I. M. Nikbin, S. R. Rahimi, and A. Heidarpour, "A new approach to determine strength of perfobond rib shear connector in steel-concrete composite structures by employing neural network," *Engineering Structures*, vol. 157, pp. 235–249, 2018.
- [17] Y. Liu, H. Xin, and Y. Liu, "Experimental and analytical study on shear mechanism of rubber-ring perfobond connector," *Engineering Structures*, vol. 197, Article ID 109382, 2019.
- [18] W. H. Bai and B. X. Sun, "Experimental study on flexural behavior of recycled coarse aggregate concrete beam," *Applied Mechanics and Materials*, vol. 29–32, pp. 543–548, 2010.
- [19] X. Wang, Y. Liu, and Y. Liu, "Experimental study on shear behavior of notched long-hole perfobond connectors," *Advances in Structural Engineering*, vol. 22, no. 1, pp. 1–12, 2018.
- [20] L. Xiao, *Study of Static and Fatigue Behavior of PBL Shear Connectors in Steel-Concrete Composite Structure*, Southwest Jiaotong University, Chengdu, China, 2012, in Chinese.
- [21] Y. Liu, H. Xin, and Y. Liu, "Load transfer mechanism and fatigue performance evaluation of suspender-girder composite anchorage joints at serviceability stage," *Journal of Constructional Steel Research*, vol. 145, pp. 82–96, 2018.
- [22] Y. Yang and Y. Chen, "Experimental study on the shear capacity of PBL shear connectors," *Engineering Mechanics*, vol. 35, no. 9, pp. 89–96, 2018, in Chinese.
- [23] B. Zhu and X. Wang, "Experimental study on PBL shear connectors of steel-concrete composite bridge considering transverse prestressing," *Journal of South Jiaotong University*, vol. 51, no. 4, pp. 621–631, 2016, in Chinese.
- [24] W. Wang, Q. Li, C. Zhao, and W. Zhang, "Study on load-slip characteristic curve of perfobond shear connectors in hybrid structures," *Engineering Mechanics*, vol. 32, no. 3, pp. 57–65, 2015, in Chinese.
- [25] Z. Jiang and Y. Wang, "Experimental study of mechanical properties of large size PBL shear connectors for hybrid girder bridge," *Bridge Construction*, vol. 48, no. 1, pp. 36–41, 2018, in Chinese.
- [26] J. Di, Y. Zou, X. Zhou, F. Qin, and X. Peng, "Push-out test of large perfobond connectors in steel-concrete joints of hybrid bridges," *Journal of Constructional Steel Research*, vol. 150, pp. 415–429, 2018.
- [27] S. Zheng, Y. Liu, T. Yoda, and W. Lin, "Parametric study on shear capacity of circular-hole and long-hole perfobond shear connector," *Journal of Constructional Steel Research*, vol. 117, pp. 64–80, 2016.
- [28] C. Liu, Z. Lv, C. Zhu, G. Bai, and Y. Zhang, "Study on calculation method of long term deformation of RAC beam based on creep adjustment coefficient," *KSCE Journal of Civil Engineering*, vol. 23, no. 1, pp. 260–267, 2019.
- [29] EUROCODE 4, *EN 1994-1-1. Design of Composite Steel and Concrete Structures Part 1.1 General Rules and Rules for Buildings*, CEN-European Committee for Standardization, Brussels, Belgium, 2005.
- [30] GB/T1499.2-2018, *Steel for the Reinforcement of Concrete—Part 2: Hot Rolled Ribbed Bars*, China standardization administration, Beijing, China, 2018, in Chinese.
- [31] ABAQUS, *ABAQUS 6.9 Analysis User's Manual*, 2008.
- [32] P. Baltay and A. Gjelsvik, "Coefficient of friction for steel on concrete at high normal stress," *Journal of Materials in Civil Engineering*, vol. 2, no. 1, pp. 46–49, 1990.
- [33] F. Ding, X. Ying, L. Zhou, and Z. Yu, "Unified calculation method and its application in determining the uniaxial mechanical properties of concrete," *Frontiers of Architecture and Civil Engineering in China*, vol. 5, no. 3, pp. 381–393, 2011.



Hindawi

Submit your manuscripts at
www.hindawi.com

